















An x-ray penumbral imager for measurements of electron-temperature profiles in inertial confinement fusion implosions at OMEGA

Cite as: Rev. Sci. Instrum. **92**, 043548 (2021); <https://doi.org/10.1063/5.0041038>

Submitted: 18 December 2020 . Accepted: 03 April 2021 . Published Online: 22 April 2021

 P. J. Adrian,  J. Frenje, B. Aguirre,  B. Bachmann,  A. Birkel,  M. Gatu Johnson,  N. V. Kabadi, B. Lahmann, C. K. Li,  O. M. Mannion, W. Martin,  Z. L. Mohamed, S. P. Regan,  H. G. Rinderknecht,  B. Scheiner,  M. J. Schmitt, F. H. Séguin, R. C. Shah,  H. Sio, C. Sorce,  G. D. Sutcliffe, and  R. D. Petrasso

COLLECTIONS

Paper published as part of the special topic on [Proceedings of the 23rd Topical Conference on High-Temperature Plasma Diagnostics](#)



View Online



Export Citation



CrossMark

ARTICLES YOU MAY BE INTERESTED IN

[A multi-channel x-ray temporal diagnostic for measurement of time-resolved electron temperature in cryogenic deuterium-tritium implosions at OMEGA](#)



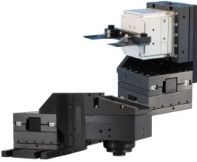
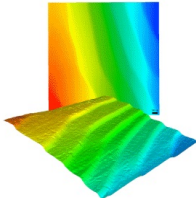
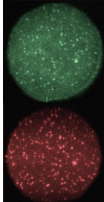
Review of Scientific Instruments **92**, 023507 (2021); <https://doi.org/10.1063/5.0042329>

[Yield degradation due to laser drive asymmetry in D³He backlit proton radiography experiments at OMEGA](#)

Review of Scientific Instruments **92**, 043551 (2021); <https://doi.org/10.1063/5.0043004>

[High-energy-density-physics measurements in implosions using Bayesian inference](#)

Physics of Plasmas **28**, 032703 (2021); <https://doi.org/10.1063/5.0040616>

 <p>MAD CITY LABS INC. www.madcitylabs.com</p>	<p>Nanopositioning Systems</p> 	<p>Modular Motion Control</p> 	<p>AFM and NSOM Instruments</p> 	<p>Single Molecule Microscopes</p> 
---	--	--	---	--

An x-ray penumbral imager for measurements of electron-temperature profiles in inertial confinement fusion implosions at OMEGA

Cite as: Rev. Sci. Instrum. 92, 043548 (2021); doi: 10.1063/5.0041038

Submitted: 18 December 2020 • Accepted: 3 April 2021 •

Published Online: 22 April 2021



View Online



Export Citation



CrossMark

P. J. Adrian,^{1,a)} J. Frenje,¹ B. Aguirre,² B. Bachmann,³ A. Birkel,¹ M. Gatu Johnson,¹ N. V. Kabadi,¹ B. Lahmann,¹ C. K. Li,¹ O. M. Mannion,⁴ W. Martin,² Z. L. Mohamed,⁴ S. P. Regan,⁴ H. G. Rinderknecht,⁴ B. Scheiner,⁵ M. J. Schmitt,⁵ F. H. Séguin,¹ R. C. Shah,⁴ H. Sio,³ C. Sorce,⁴ C. D. Sutcliffe,¹ and R. D. Petrasso¹

AFFILIATIONS

¹Plasma Science and Fusion Center: MIT, Cambridge, Massachusetts 02139, USA

²Sandia National Laboratories, Albuquerque, New Mexico 87185, USA

³Lawrence Livermore National Laboratory, Livermore, California 94550, USA

⁴Laboratory for Laser Energetics: University of Rochester, Rochester, New York 14623, USA

⁵Los Alamos National Laboratory, Los Alamos, New Mexico 87544, USA

Note: Paper published as part of the Special Topic on Proceedings of the 23rd Topical Conference on High-Temperature Plasma Diagnostics.

a) Author to whom correspondence should be addressed: pjadrian@mit.edu

ABSTRACT

Hot-spot shape and electron temperature (T_e) are key performance metrics used to assess the efficiency of converting shell kinetic energy into hot-spot thermal energy in inertial confinement fusion implosions. X-ray penumbral imaging offers a means to diagnose hot-spot shape and T_e , where the latter can be used as a surrogate measure of the ion temperature (T_i) in sufficiently equilibrated hot spots. We have implemented a new x-ray penumbral imager on OMEGA. We demonstrate minimal line-of-sight variations in the inferred T_e for a set of implosions. Furthermore, we demonstrate spatially resolved T_e measurements with an average uncertainty of 10% with 6 μm spatial resolution.

Published under license by AIP Publishing. <https://doi.org/10.1063/5.0041038>

I. INTRODUCTION

One of the main challenges of inertial confinement fusion (ICF) is symmetry control of the forming hot spot surrounded by a converging cold shell.^{1–3} Understanding asymmetries in both the hot spot and shell is essential as they impact the implosion performance. Asymmetries also generate bulk flows that degrade the conversion of shell kinetic energy into hot-spot thermal energy.^{4,5} Measurements of hot-spot shape and thermal temperature are therefore critical for understanding the performance of an ICF implosion. Recently, penumbral imaging of hot-spot x-ray emission was used at the National Ignition Facility (NIF) to simultaneously measure hot-spot shape and thermal temperature to assess asymmetry in different implosion designs,^{6,7} as well as spatially resolved

electron temperature in order to quantify mix-induced radiative cooling.⁸

Penumbral imaging is a coded imaging technique where an emitting source of size S is imaged with an aperture of radius R_{app} such that $2R_{app} > S$. This imaging technique is used when signal statistics prevent the use of conventional pinhole imaging ($2R_{app} \ll S$).⁶ Penumbral images consist of two regions: the umbra where information about the total emission is encoded and the penumbra where information about spatial distribution of the emitting source is encoded. For x-ray imaging, the umbra of differentially filtered images is used to reconstruct the bremsstrahlung spectrum from which the electron temperature (T_e) is inferred.⁷

We have developed and fielded a new penumbral imager at the OMEGA Laser Facility, with 6 μm resolution, to image x rays in

the energy range of 10–30 keV. This system is based on the same hardware used for the existing charged particle penumbral imaging system.^{9–11} Three imagers can be fielded in different 10-in. diagnostic manipulators (TIMs) to study 3D asymmetries. We record images in different x-ray energy bands using a filtered stack of FujiTM image plates. In this contribution, we detail an error analysis for determining T_e from penumbral images recorded. We demonstrate that the measured T_e is independent of line of sight. We also discuss in detail the technique to measure $T_e(r)$.

This paper is organized as follows: Section II describes the design of the penumbral imager. Section III presents the analysis of inferring spatially averaged T_e . Section IV discusses a method used to infer the spatial T_e profile.

II. PENUMBRA-IMAGER DESIGN

The x-ray penumbral imager used in this work is based on hardware from the penumbral charged particle imaging systems.^{9–11} These imagers are TIM based diagnostics that hold an aperture of 4.2 cm from the target-chamber center. The system has a clear line of sight to a detector plane fixed at 59 cm from the aperture, yielding a magnification of ~ 14 [Fig. 1(a)]. Currently, there are three types of compatible apertures: $1 \times 2000 \mu\text{m}^2$, $19 \times 400 \mu\text{m}^2$, or $151 \times 100 \mu\text{m}^2$ (number of pinholes \times diameter) made from a substrate of $500 \mu\text{m}$ thick tantalum, $125 \mu\text{m}$ thick tungsten, or $125 \mu\text{m}$ thick tungsten, respectively. All apertures have an out of circularity $< 3 \mu\text{m}$. The

detector is an array of FujiTM SR x-ray image plates. The spatial resolution of the system at a magnification of 14 is $6 \mu\text{m}$, calculated from Eq. (1) of Ref. 6 assuming a detector resolution of $60 \mu\text{m}$ for SR-type image plates. The spatial resolution is limited by the combination of detector resolution and x-ray diffraction.

The three apertures cover a design space based on the x-ray emission size. Capsules imploded at OMEGA have radii that vary from 200 to $600 \mu\text{m}$, which produce hot spots from 20 to $150 \mu\text{m}$ in radius. In certain experiments, it is desirable to image the coronal emission, which typically occurs at a radius comparable to the initial radius of the capsule. Asymmetries in the hard x-ray coronal emission (10–30 keV) are correlated with drive asymmetries, which can result from laser miss-pointing, capsule defects, or the stalk that holds the capsule. For this application, the $1 \times 2000 \mu\text{m}^2$ diameter pinhole is typically used. In cases where the coronal emission is either not of interest or dim compared to the hot spot, the $19 \times 400 \mu\text{m}^2$ or $151 \times 100 \mu\text{m}^2$ aperture is used for hot-spot imaging. Using the multiple-pinhole designs enables differential filtering on the detector plane to record images of the hot spot in different energy bands, which are used to reconstruct $T_e(r)$. Typically, the $19 \times 400 \mu\text{m}^2$ aperture design is used to image exploding-pusher-type implosions because they can produce hot spots of $\sim 100 \mu\text{m}$ in radius, while the $151 \times 100 \mu\text{m}^2$ aperture design is used to image cryogenic implosions, which produce hot spots of $30 \mu\text{m}$ in radius.

The penumbral data from shot 95512 are shown in Fig. 1(c), with the target and laser drive described in the caption. Four image

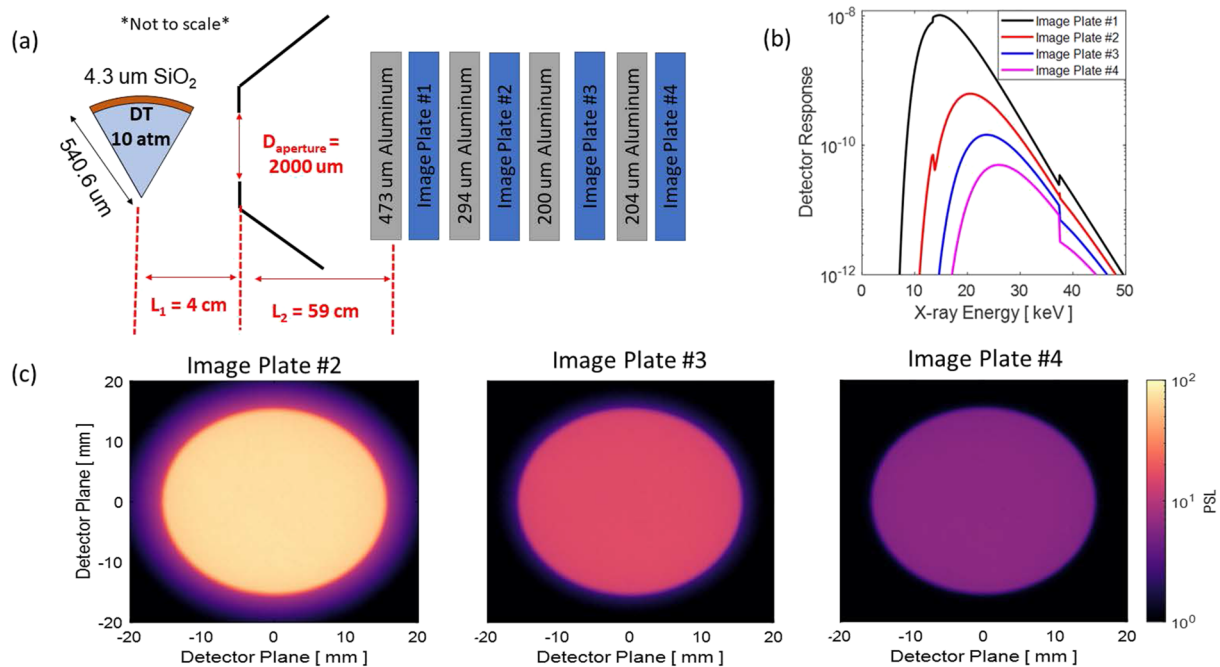


FIG. 1. (a) Diagram of the x-ray penumbral imager as fielded on shot 95512. The capsule had a $541 \mu\text{m}$ radius with a $4.3 \mu\text{m}$ thick glass shell filled with 10 atm of equimolar DT and was compressed by 28 kJ of laser energy in a 1-ns square pulse. A $2000 \mu\text{m}$ diameter aperture was used at $14\times$ magnification. Four image plates were fielded in a filter stack with various thicknesses of aluminum. (b) Calculated detector response (arbitrary units) of each image plate to incident x rays. The detector response is given by $IP_{\text{sen}}(E) \times T_k(E) \times j(E)/E$, where $j(E)$ is the thermal bremsstrahlung spectrum with $T_e = 4.0 \text{ keV}$. (c) Measured x-ray penumbral images for the second, third, and fourth image plates. The first image plate is saturated due to high x-ray flux and is not shown.

plates were fielded in a filter stack arrangement detailed in panel (a). Figure 1(b) shows the detector spectral sensitivity calculated for a $T_e = 4.0$ keV thermal bremsstrahlung spectrum, which best describes the source spectrum (as discussed in Sec. III). The four images are most sensitive to 14, 19, 22, and 26 keV x rays. The image plates were scanned with $25 \mu\text{m}$ resolution at a latitude of 5 with 537 V bias on the photo-multiplier of the scanning system.

III. BURN AVERAGED ELECTRON TEMPERATURE

A burn averaged T_e is extracted from the inferred x-ray spectrum that is derived from the energy deposited in the umbra of each penumbral image (filtered differently). The image plate scanner measures the photo-stimulated luminescence (PSL), which is related to the energy deposited in the phosphor layer. The PSL recorded in the umbra of the k th image plate is calculated as

$$PSL_k = \int_0^\infty \frac{IP_{sen}(E) j(E)}{F_k(t) E} T_k(E) dE, \quad (1)$$

where E is the x-ray energy, $IP_{sen}(E)$ is the image plate sensitivity in PSL/photon, $F_k(t)$ represents the fading of the image plate when it is scanned t minutes after exposure, $j(E)/E$ is the photon emission in photons/keV, and $T_k(E)$ is the transmission function of all filters in front of the k th image plate. In this work, the spectrum is modeled using a single temperature bremsstrahlung emission model $j(E) = A \exp(-E/T_e)$, where A and T_e are the fit variables. For the implosion reported in this paper, opacity effects are negligible.

The set of penumbral images displayed in Fig. 1 was analyzed to extract a burn averaged T_e . The error analysis was done with a Monte-Carlo method, which conducted one thousand trials to infer T_e . Four sources of error were considered in the analysis, and below is a brief description of each error source. First, the measured PSL in the umbra of the three image plates was 74.1 ± 1.5 , 15.9 ± 0.3 , and 5.7 ± 0.2 PSL. The error in these numbers represents the $1 - \sigma$ standard deviation from the variation in PSL recorded in the umbra. The PSL variation in the umbra is representative of the photon statistics in the measurement. Second, the image-plate sensitivity is known to vary between different image plates. Rosenberg *et al.*¹² measured sensitivity variations of the SR-type image plate. The measured variations in $IP_{sen}(E)$ for SR image plates were found to be well modeled by fitting Eq. (2) from Ref. 12 to measurements (for more information on this model see Ref. 12 and references within). Third, each image plate has variations in its fade curve. Maddox *et al.*¹³ measured the variation of SR-type image plate fade curves. The SR-type image plate fade curve is well described by a series of two decaying exponentials with coefficients given in Table II in Ref. 13. Finally, the transmission curves for each filter material were calculated using the NIST database using the measured filter thickness. The uncertainty in the measured filter thickness was 2%. These four sources were considered to be independent of each other and randomly distributed, given the measured uncertainties in each when quantifying the error in the inferred T_e . Figure 2 displays the results of the Monte-Carlo error calculation with the histogram of the inferred T_e values. Overlaid in black is a Gaussian fit to the histogram, indicating that the burn averaged electron temperature is $T_e = 4.0 \pm 0.2$ keV. In addition, each error source is overlaid with its relative contribution to the total error. From this analysis, it is clear that the main sources of

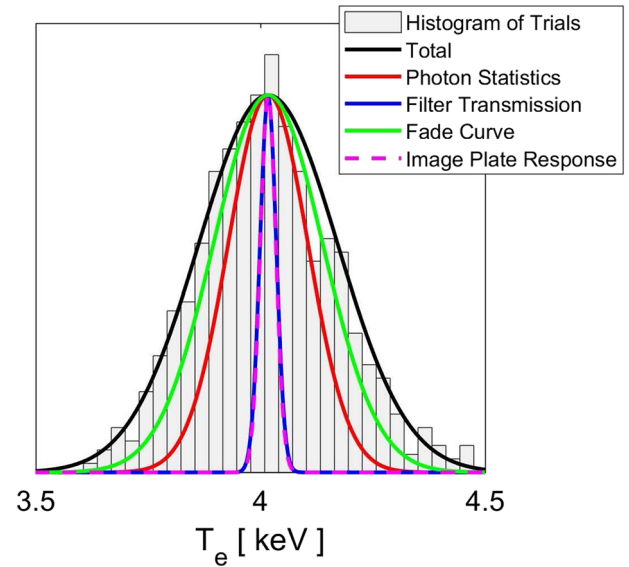


FIG. 2. Histogram reflecting the error in the inferred T_e from the penumbral data in Fig. 1(c). The relative contribution to the uncertainty in the measured T_e due to photon statistics, filter transmission, image plate sensitivity, and fade curve is labeled.

error in the inferred T_e are from photon statistics and uncertainty in the fade curve of each image plate.

Shot 95512 was one of the series of implosions where two penumbral imagers were fielded in TIM3 and TIM5 with similar setups as displayed in Fig. 1(a). The burn averaged T_e for both imagers is shown in Fig. 3. As shown, both detectors are in agreement with each other spanning a wide T_e -range. The T_e -range was

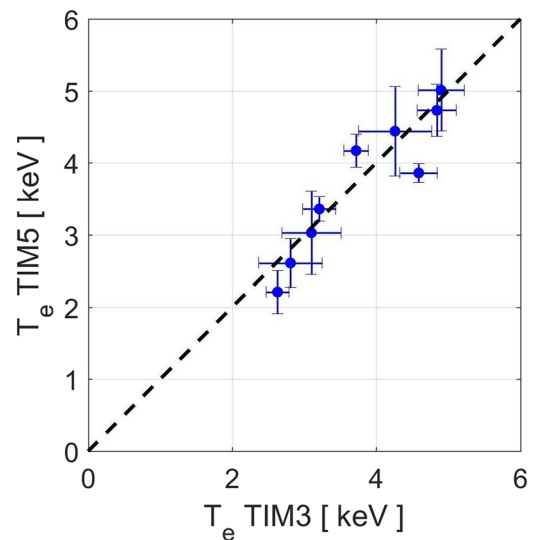


FIG. 3. Burn averaged T_e measured on the TIM5 and TIM3 line of sight for a series of shots 95495 through 95514. The range of T_e resulted from a variation of the laser energy and capsule fill pressures in this shot series.

obtained by varying the laser intensity on capsules from 5×10^{14} to 1.20×10^{15} W/cm², as well as changing the fill density of the capsules.

IV. MEASUREMENTS OF ELECTRON-TEMPERATURE PROFILE

The source profile must be reconstructed from the measured penumbral image. Currently, there exists a bevy of reconstruction algorithms to determine the source image from a penumbral image.^{14–18} In this work, we used a deconvolution approach based on the Lucy–Richardson (LR) algorithm.¹⁹ This approach is an iterative maximum likelihood algorithm, which projects the aperture function onto the detector plane and deconvolves it from the recorded penumbral image. At every iteration, the source image is convolved with the aperture function and compared against the measured penumbral image using a chi-squared metric. The iterations stop once the reduced chi-square metric is of the order of unity or lower. One weakness of the LR algorithm is noise amplification. However, for x-ray penumbral imaging, we have found that signal statistics is excellent for x rays in the energy range of 10–30 keV for most implosions of interest.

Figure 4 shows an example of image reconstructions from two penumbral images collected on a thin-glass capsule implosion. Details about the capsule dimensions, gas fill, laser drive, penumbral aperture, and filters are given in the figure caption. Two measured x-ray penumbral images are shown in Figs. 4(a) and 4(b). The LR algorithm was used to reconstruct the source. Both images converged to the solution shown in Figs. 4(c) and 4(d) in

100 iterations. The images in (c) and (d) both show a ring-like structure. This structure results from the unablated glass shell that remains surrounding the hot spot. The oxygen and silicon dominate the x-ray signal due to both higher density and Z^2 when compared to that of the hot spot, which is comprised of DT³He.

From these measurements, the radial profile of T_e is also determined. We assume the spherical symmetry of the source, which allows the reconstructed x-ray images to be azimuthally averaged to get the brightness profile. Figure 4(e) shows the radial brightness profiles from (c) and (d). The radial brightness profiles were obtained using a radial grid spacing twice the predicted spatial resolution, or 12 μ m. The errors in the brightness profiles are determined from the azimuthal variation in each radial bin. It is important to emphasize that the brightness profile is a chord-integrated quantity. To extract $T_e(r)$, we calculate the radial emission from the brightness profiles by an inverse Abel transform. We use a discrete version of the Abel transform proposed by Yoshikawa and Suto²⁰ to calculate the radial x-ray emission profiles shown in (f) from the brightness profiles displayed in (e) of Fig. 4.

The relative amplitude of the radial emission profiles of the two images is used to infer T_e in each radial bin by using Eq. (1) and the known filtering of the two images. Figure 5 shows the inferred $T_e(r)$ for shot 98963. A post-shot simulation of this implosion was performed using the HYADES 1D radiation hydrodynamics code,²¹ and the emission-averaged $T_e(r)$ is shown by the blue solid line in Fig. 5 for comparison. As shown, the measured $T_e(r)$ agrees with the simulation. Generally, the uncertainty in $T_e(r)$ on average is 10%. The best inference of the temperature is where the most x-ray emission occurs. However, there are large uncertainties

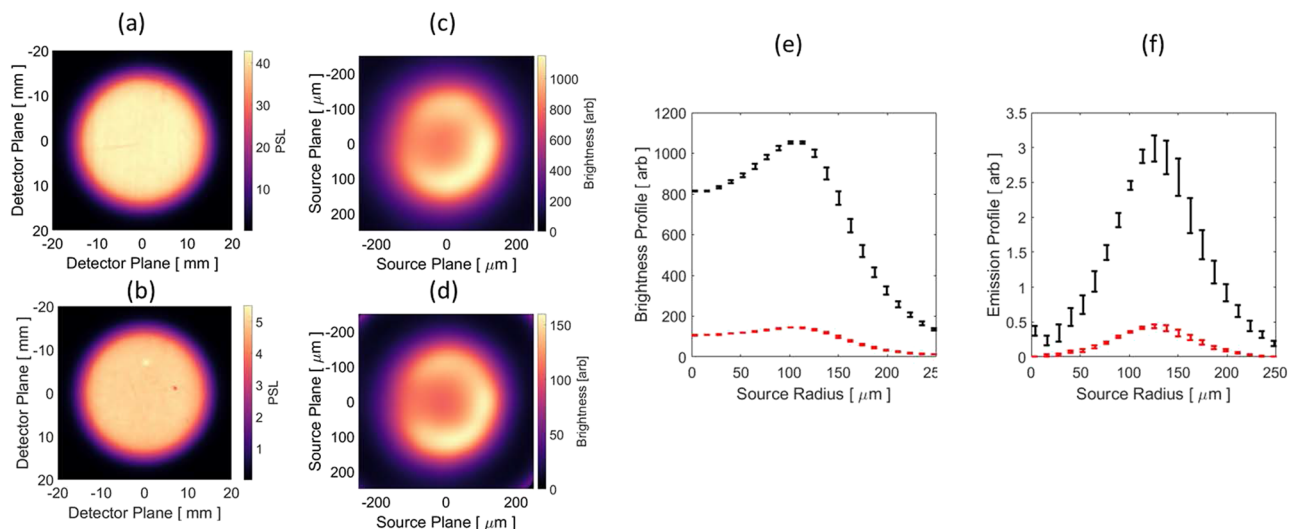


FIG. 4. Data from shot 98963 that had a capsule with 422 μ m radius with a glass shell thickness of 2.4 μ m filled with 10 atm D₂, 15 atm ³He, and ~ 0.04 atm T₂ imploded with 15.6 kJ of laser energy in a 0.6 ns square pulse. The x-ray penumbral imager used a 1000 μ m radius aperture at 14 \times magnification and fielded two image plates in a single stack. (a) Recorded x-ray penumbral image closest to TCC. The filter in the front contains 15 μ m tantalum + 3000 μ m CR-39 (C₁₂H₁₈O₇) + 100 μ m aluminum. (b) X-ray penumbral image for the image plate furthest from TCC. This image had an additional 150 μ m aluminum in the front. (c) and (d) Reconstructed x-ray emission obtained from (a) and (b), respectively. (e) Azimuthally averaged brightness profiles (chord integrated) from (c) and (d) in black and red, respectively. (f) Radial emission profiles calculated from the surface brightness profiles in (e) via Abel inversion.

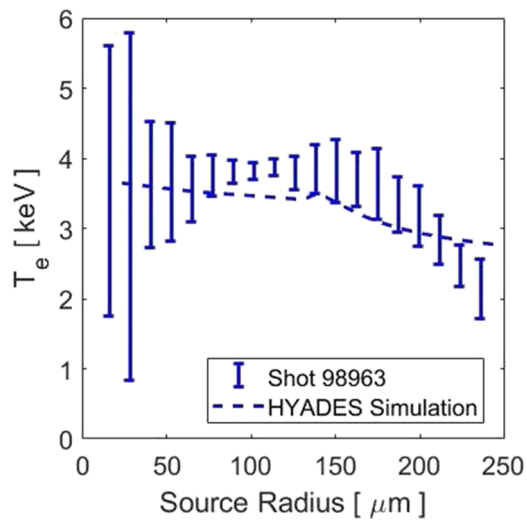


FIG. 5. Measured $T_e(r)$ for shot 98963 (blue data points). $T_e(r)$ is inferred from the x-ray emission histories shown in Fig. 4(f). A post-shot HYADES simulation is shown (blue dashed line). The simulated T_e is an x-ray emission averaged over the entire implosion time.

at small radii, which is due to low levels of emission occurring at small radii.

V. CONCLUSIONS AND OUTLOOK

In conclusion, we have implemented a new x-ray penumbral imaging diagnostic at OMEGA with $6\ \mu\text{m}$ spatial resolution capable of spatially resolved T_e measurements with an average error of 10%. The system probes x rays between 10 and 30 keV. This measurement technique has applications such as charged-particle-stopping-power measurement^{22,23} and diagnosis of the performance of several types of ICF implosions.⁷ Future work on this diagnostic will be to develop techniques that utilize three lines of sight simultaneously to reconstruct 3D maps of electron temperature.

ACKNOWLEDGMENTS

This work was supported by the U.S. Department of Energy under Grant No. DE-NA0003868, the Laboratory for Laser Energetics under Grant No. 417532G/UR FAO GR510907, and the National Laser Users' Facility under Grant No. DE-NA0003938. P.J.A. was supported under Grant No. DE-NA0003960. The views and opinions of authors expressed herein do not necessarily state or reflect those of the United States Government or any agency thereof.

DATA AVAILABILITY

The data that support the findings of this study are available from the corresponding author upon reasonable request.

REFERENCES

- J. Lindl, *Phys. Plasmas* **2**, 3933 (1995).
- S. W. Haan *et al.*, *Phys. Plasmas* **18**, 051001 (2011).
- A. B. Zylstra *et al.*, *Phys. Plasmas* **22**, 056301 (2015).
- M. Gatu Johnson *et al.*, *Phys. Plasmas* **20**, 042707 (2013).
- M. Gatu Johnson *et al.*, *Phys. Rev. E* **94**, 021202(R) (2016).
- B. Bachmann *et al.*, *Rev. Sci. Instrum.* **87**, 11E201 (2016).
- L. C. Jarrott *et al.*, *Rev. Sci. Instrum.* **87**, 11E534 (2016).
- B. Bachmann *et al.*, *Phys. Rev. E* **101**, 033205 (2020).
- F. H. Séguin *et al.*, *Rev. Sci. Instrum.* **75**, 3520 (2004).
- J. L. DeCiantis *et al.*, *Rev. Sci. Instrum.* **77**, 043503 (2006).
- F. H. Séguin *et al.*, *Phys. Plasmas* **23**, 032705 (2016).
- M. J. Rosenberg *et al.*, *Rev. Sci. Instrum.* **90**, 013506 (2019).
- B. R. Maddox *et al.*, *Rev. Sci. Instrum.* **82**, 023111 (2011).
- B. Bachmann, "X-ray penumbral imaging diagnostic developments at the National Ignition Facility," *Proc. SPIE* **10390**, 103900B (2017).
- F. H. Séguin *et al.*, *Phys. Plasmas* **13**, 082704 (2006).
- T. Ueda, S. Fujioka, S. Nozaki, Y.-W. Chen, and H. Nishimura, *J. Phys.: Conf. Ser.* **244**, 032061 (2010).
- R. Azuma, S. Nozaki, S. Fujioka, Y. W. Chen, and Y. Namihira, *Rev. Sci. Instrum.* **81**, 10E517 (2010).
- P. L. Volegov *et al.*, *Phys. Plasmas* **25**, 062708 (2018).
- W. H. Richardson, *J. Opt. Soc. Am.* **62**, 55 (1972).
- K. Yoshikawa and Y. Suto, *Astrophys. J.* **513**, 549 (1999).
- J. T. Larsen and S. M. Lane, *J. Quant. Spectrosc. Radiat. Transfer* **51**, 179 (1994).
- J. Frenje *et al.*, *Phys. Rev. Lett.* **115**, 205001 (2015).
- J. Frenje *et al.*, *Phys. Rev. Lett.* **122**, 015002 (2019).